Accepted Article

Title: N2 Electroreduction to NH3 via Selenium Vacancy-Rich ReSe2 Catalysis at an Abrupt Interface

Authors: Feili Lai, Wei Zong, Guanjie He, Yang Xu, Haowei Huang, Bo Weng, Dewei Rao, Johan A. Martens, Johan Hofkens, Tianxi Liu, and Ivan P. Parkin

This manuscript has been accepted after peer review and appears as an Accepted Article online prior to editing, proofing, and formal publication of the final Version of Record (VoR). This work is currently citable by using the Digital Object Identifier (DOI) given below. The VoR will be published online in Early View as soon as possible and may be different to this Accepted Article as a result of editing. Readers should obtain the VoR from the journal website shown below when it is published to ensure accuracy of information. The authors are responsible for the content of this Accepted Article.

WILEY-VCH

RESEARCH ARTICLE

N₂ Electroreduction to NH₃ via Selenium Vacancy-Rich ReSe₂ Catalysis at an Abrupt Interface

Feili Lai,[a,d] Wei Zong,[a] Guanjie He,[c] Yang Xu,[c] Haowei Huang,[d] Bo Weng,[d] Dewei Rao,[f*] Johan A. Martens,[e] Johan Hofkens,[b,d] Ivan P. Parkin,[c*] and Tianxi Liu[a*]

[a]   Dr. F.L. Lai, W. Zong, Prof. T.X. Liu
        The Key Laboratory of Synthetic and Biological Colloids, Ministry of Education, School of Chemical and Material Engineering, Jiangnan University, Wuxi
        214122, P. R. China
        Email: txliu@jiangnan.edu.cn
[b]   Prof. J. Hofkens
        Max Planck Institute for Polymer Research, Ackermannweg 10, 55128 Mainz, Germany
[c]   Dr. G.J. He, Dr. Y. Xu, Prof. I.P. Parkin
        Christopher Ingold Laboratory, Department of Chemistry, University College London, 20 Gordon Street, London WC1H 0AJ, UK
        Email: i.p.parkin@ucl.ac.uk
[d]   Dr. F.L. Lai, H.W. Huang, Dr. B. Weng, Prof. J. Hofkens
        Department of Chemistry, KU Leuven, Celestijnenlaan 200F, Leuven 3001, Belgium
[e]   Prof. J.A. Martens
        Centre of Surface Chemistry and Catalysis: Characterisation and Application team, KU Leuven, Leuven, 3001, Belgium
[f]   Dr. D.W. Rao
        School of Materials Science and Engineering, Jiangsu University, Zhenjiang 212013, P. R. China
        Email: dewei@ujs.edu.cn

        Supporting information for this article is given via a link at the end of the document.

Abstract: Vacancy engineering has been proved repeatedly as an adoptable strategy to boost electrocatalysis, while its poor selectivity restricts the usage in nitrogen reduction reaction (NRR) as overwhelming competition from hydrogen evolution reaction (HER). Revealed by density functional theory calculations, the selenium vacancy in ReSe₂ crystal can enhance its electroactivity for both NRR and HER by shifting the *d*-band from -4.42 to -4.19 eV. To restrict the HER, we report a novel method by burying selenium vacancy-rich ReSe₂@carbonized bacterial cellulose (Vᵣ-ReSe₂@CBC) nanofibers between two CBC layers, leading to boosted Faradaic efficiency of 42.5 % and ammonia yield of 28.3 μg h⁻¹ cm⁻² at a potential of -0.25 V on an abrupt interface. As demonstrated by the nitrogen bubble adhesive force, superhydrophilic measurements, and COMSOL Multiphysics simulations, the hydrophobic and porous CBC layers can keep the internal Vᵣ-ReSe₂@CBC nanofibers away from water coverage, leaving more unoccupied active sites for the N₂ reduction (especially for the potential determining step of proton-electron coupling and transferring processes as *HNNH₂ → *H₂NNH₂).

Introduction

Ammonia (NH₃) is not only a vital feedstock to manufacture fertilizers, pharmaceutical and chemical products,[1-3] but also a promising energy carrier with high hydrogen density and low liquefying pressure,[4] making the fixation of the inexhaustible nitrogen (N₂) into NH₃ a key transformation. However, N₂ fixation is still severely confined by the thermodynamic stability of the N₂ molecule and the absence of a permanent dipole in the N≡N triple bond.[5,6] As a century-old N₂ fixation method, the Haber-Bosch process occupies an important industrial position in NH₃ manufacture, which requires both iron-based catalysts and harsh operating conditions (400-600 °C and 150-350 atm).[7] As a consequence, 1.4 % of the world's energy consumption is used in the Haber-Bosch process, leading to 1.6 % of total global CO₂ emission,[8,9] which makes the exploration of sustainable N₂ fixation systems under ambient conditions an important issue.[10,11]

Electrochemical N₂ reduction reaction (NRR) emerges as an alternative technology to fix nitrogen into ammonia at ambient conditions.[12-14] This can be powered by renewable energy from electrochemical cells and operate by using versatile hydrogen atoms as alternative sources.[15,16] Until now, the development of NRR is mainly focused on exploring advanced electrocatalysts to activate dinitrogen for alleviated energy barriers.[17,18] Among them, transition metal based electrocatalysts are regarded as promising species towards the NRR process,[19-23] due to their available *d*-orbital electrons for *π*-back donation process. However, their practical applications are still hindered by low NH₃ yield and Faradaic efficiency, which originates from the following two perspectives: (1) the binding force between transition metals and nonpolar dinitrogen is too weak to break the strong N≡N triple bond due to the poorly optimized structure of the electrocatalyst;[24] (2) the adverse hydrogen evolution reaction HER) is regarded as an intense-competing reaction towards NRR due to the preferential adsorption of the hydrogen (H) atom over a nitrogen (N) atom.[8,25] For an enhanced interfacial force towards nitrogen, one effective strategy is to tailor the electronic structure of the transition metal based electrocatalysts by incorporating defect structures (such as anionic vacancies). The existence of anionic vacancies may change the charge distribution and activate the transition metals near the vacancies, leading to an increased number of active sites for enhanced NRR process with stronger N-metal interaction. For instance, Sun *et al.* found that the defect-rich transition metal dichalcogenide MoS₂ with a flower-like structure shows outstanding electrocatalysis for N₂ reduction to NH₃, as compared to the defect-free counterpart.[23] However, the as-incorporated defect structures may also be beneficial for achieving a stronger proton-metal interaction for an accelerated HER process.[26,27] This reaction is an intense competitor towards NRR, and hence would significantly decrease the effective number of active sites for N₂ adsorption and activation. Recently, Ling *et al.* designed a new NRR electrocatalyst by introducing a superhydrophobic layer of zeolitic imidazolate framework-71 over the surface of a NRR electrocatalyst, which realized a significant boost in Faradic efficiency (10 percent increase) by suppressing the HER process.[25] Therefore, it becomes a key issue in combining defect engineering (such as anion vacancies) in transition metal-based electrocatalysts with an optimized three-phase boundary, but not change the N₂ transmission to the

defect-rich surface and reduce its number of active sites for N_2 adsorption/activation.

Herein, we report an efficient and selective NRR process under ambient conditions by sandwiching selenium vacancy-rich $ReSe_2$@carbonized bacterial cellulose (V_r-$ReSe_2$@CBC) nanofibers between two hydrophobic CBC layers. Density functional theory (DFT) calculations demonstrate that defect engineering could enhance the electrocatalytic properties of $ReSe_2$ by positively shifting its *d*-band center but show poor selectivity towards nitrogen reduction and hydrogen evolution reactions. Interestingly, the competition from HER process can be suppressed by covering hydrophobic CBC layers on both sides of V_r-$ReSe_2$@CBC nanofibers, resulting in a boosted Faradaic efficiency of 42.5 % and a maintained NH_3 yield of 28.3 µg h^{-1} cm^{-2} at room temperature. The detailed advantages for the "sandwich"-structured CBC/V_r-$ReSe_2$@CBC/CBC membrane were further unveiled by under-electrolyte nitrogen bubble adhesive force tests, contact angle measurements, and COMSOL Multiphysics simulations from experimental and theoretical approaches.

Results and Discussion

The selenium vacancy-rich rhenium diselenide nanosheets were anchored on the surface of carbonized bacterial cellulose nanofibers (Figure S1 & S2) by combining hydrothermal synthesis and heat treatment (Ar gas, 700 °C for 3 h; Figure 1a), denoted as selenium vacancy-rich $ReSe_2$@CBC (V_r-$ReSe_2$@CBC) nanofibers (NFs). In comparison, vacancy-poor $ReSe_2$@CBC (V_p-$ReSe_2$@CBC) NFs were prepared by annealing hydrothermally-synthesized $ReSe_2$@CNC NFs under a Se-rich atmosphere. The transmission electron microscopy (TEM) image for V_r-$ReSe_2$@CBC NFs (Figure 1b) exhibits abundant nanofibrous integrities with diameters of ~30 nm. According to this hybridization strategy, the V_r-$ReSe_2$@CBC NFs would deliver a higher specific surface area of 55.4 m^2 g^{-1} and abundant micro-/mesopores from the nitrogen physisorption isotherms (measured at -196 °C) and pore sizes distributions (Figure S3), as compared to that of 9.8 m^2 g^{-1} for $ReSe_2$ bulk with abundant aggregations (Figure S4). As clearly shown by the high-resolution TEM (HRTEM) image in Figure 1c, the amorphous CBC NFs provide a one-dimensional matrix to physically and uniformly connect highly crystalline V_r-$ReSe_2$ nanosheets with a fringe spacing of 0.64 nm, corresponding to the (100) plane of $ReSe_2$ (Inset image in Figure 2c for V_r-$ReSe_2$ model). It should be noted that the V_p-$ReSe_2$ nanosheets in V_p-$ReSe_2$@CBC NFs also possess the same fringe spacing of 0.64 nm as V_r-$ReSe_2$ nanosheets in V_r-$ReSe_2$@CBC (Figure S5), which indicates the slightly incorporated selenium vacancy in $ReSe_2$ would not obviously affect its crystal structure. The similar X-ray diffraction (XRD) patterns between V_r-$ReSe_2$@CBC and V_p-$ReSe_2$@CBC NFs (Figure S6) prove the results from HRTEM images with optimal crystal orientation of (100) plane. Specifically, six peaks at 13.3°, 31.4°, 36.4°, 42.4°, 47.1°, and 55.6° can be well indexed to the (100), (-102), (102), (300), (003), and (-421) planes for both V_r-$ReSe_2$ and V_p-$ReSe_2$ nanosheets (JCPDS: 18-1086). The TEM and corresponding energy-dispersive X-ray (EDX) elemental mapping images (Figure 1d) further demonstrate the uniform distribution of Re and Se elements along the CBC nanofibers. The EDX spectrum (Figure S7) reveals the existence of Re, Se, and C elements in

V_r-$ReSe_2$@CBC NFs, which can also be proved from the successful appearance of Re, Se, and C peaks (Figure S8 & Figure 1e) in X-ray photoelectron spectroscopy (XPS).
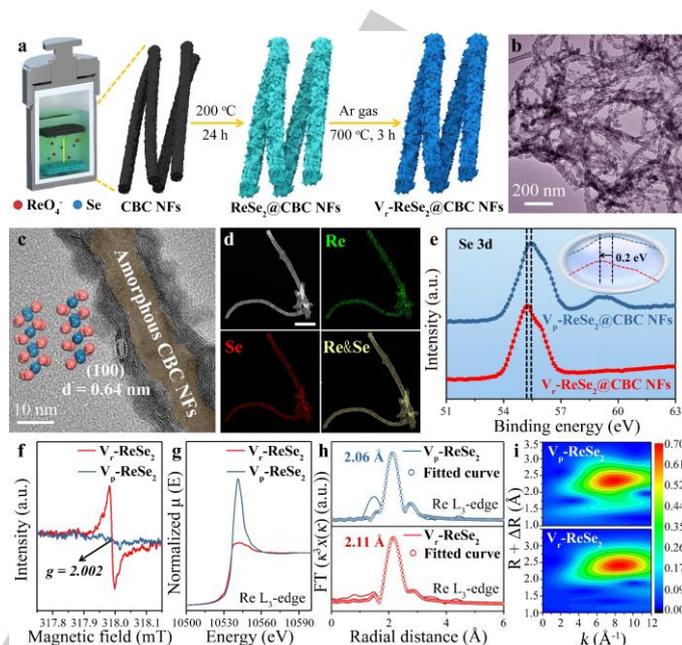

Figure 1. (a) Illustration of the fabrication of V_r-$ReSe_2$@CBC NFs. (b) TEM, and (c) HRTEM images for V_r-$ReSe_2$@CBC NFs. The light-coral and blue balls present Se and Re, respectively. (d) HAADF and corresponding EDX elemental mapping images for V_r-$ReSe_2$@CBC NFs. The scale-bar is 200 nm. (e) High resolution spectra of Se 3*d* region for V_p-$ReSe_2$@CBC and V_r-$ReSe_2$@CBC NFs. (f) EPR spectra, (g) Re L$_3$-edge XANES spectra, (h) corresponding FT-EXAFS spectra, and (i) WT-EXAFS for V_p-$ReSe_2$ and V_r-$ReSe_2$ nanosheets.

To confirm the incorporation of selenium vacancies in V_r-$ReSe_2$@CBC NFs and gain the information of local chemical environments of as-prepared materials, XPS, electron paramagnetic resonance (EPR), and synchrotron radiation technology measurements were conducted. From the XPS results firstly, two obviously characteristic peaks can be observed at 42.1 and 44.4 eV in the Re 4*f* region (Figure S8b), corresponding to the core 4*f*$_{7/2}$ and 4*f*$_{5/2}$ peaks for Re^{4+}, respectively.[28] The visible Se region at 55.2 eV (Figure 1e) strongly confirms the formation of $ReSe_2$. In addition, the Se 3*d* peak of V_r-$ReSe_2$@CBC NFs displays a negative shift of 0.2 eV to relatively lower binding energy value as compared to that of V_p-$ReSe_2$@CBC NFs, while there is no discernible variation in Re 4*f* peaks. These XPS results indicate the electron density around Se atoms is slightly increased after heat treatment under Ar gas, demonstrating the successful introduction of selenium vacancies without cationic ones. Meanwhile, the EPR investigations were applied to verify the existence of selenium vacancies within V_r-$ReSe_2$ nanosheets as such defects in semiconductors are usually paramagnetic.[29] As displayed in Figure 1f, the EPR signal at *g* = 2.002 for the V_r-$ReSe_2$ nanosheets is caused by the trapped electrons from the selenium vacancies,[30-32] while a much lower signal can be observed for the V_p-$ReSe_2$ nanosheets at the same position, demonstrating abundant selenium vacancies have been successfully incorporated into V_r-$ReSe_2$ nanosheets. Furthermore, the X-ray absorption fine structure (XAFS) spectroscopy confirms the existence of selenium vacancies. Generally speaking, the intensity of Re L$_3$-edge curve from soft X-ray absorption near-edge structure (XANES) spectroscopy is mainly depended on the nearest neighbor cation-anion bond and the number of electrons in the unoccupied state.[33-35] As the Re L$_3$-edge XANES spectra shown in Figure 1g, the obvious difference between the curves of

RESEARCH ARTICLE

V_r-ReSe$_2$ and V_p-ReSe$_2$ nanosheets indicate that the structural symmetry in V_r-ReSe$_2$ nanosheets has been partially disturbed with decreased coordination number after the incorporation of selenium vacancy. Fourier transform (FT) is a basic method for the data extraction and interpretation of EXAFS spectra.[36] The FT-EXAFS spectra of V_p-ReSe$_2$ and V_r-ReSe$_2$ nanosheets were illustrated in Figure 1h. The peak position of the corresponding Re-Se coordination for V_r-ReSe$_2$ nanosheets is slightly shifted to a higher Radial distance (2.11 Å) as compared to the V_p-ReSe$_2$ nanosheets (2.06 Å) (Figure 1h), indicating the Re-Se bond length in V_r-ReSe$_2$ nanosheets is slightly increased after incorporating selenium vacancies. In addition, the peak intensity of V_r-ReSe$_2$ nanosheets decreased slightly as compared to the V_p-ReSe$_2$ nanosheets (Figure S9). Therefore, it is proved once more that the selenium vacancies in V_r-ReSe$_2$ nanosheets would cause structural distortion,[37,38] where the detailed structure parameters are summarized from the curve fitting in Table S2 (Supporting Information). The Re-Se bond in the V_r-ReSe$_2$ nanosheets exhibit unsaturated coordination with lower coordination number (N) of 5 as compared to the V_p-ReSe$_2$ nanosheets (N = 6), which is resulted from the removal of partial Se sites from the basal plane of ReSe$_2$ nanosheets. As a very good supplement for FT, wavelet transform (WT) possesses power resolution in both k and R spaces.[39] The WT contour plots for both V_p-ReSe$_2$ and V_r-ReSe$_2$ nanosheets (Figure 1i & S10) display intensity maximums at ~8.6 Å^{-1}, indicating only one Re-Se ligand can be found at the same time without any incorporated impure ligands during preparation process.

Upon confirming the successful synthesis of V_r-ReSe$_2$@CBC NFs, we firstly evaluated the performance of perfect ReSe$_2$ and its Se vacancy one (V-ReSe$_2$) through density functional theory (DFT) calculations with detailed calculation methods in the Supporting Information. The electronic structures of ReSe$_2$ and V-ReSe$_2$, as well as their electrocatalytic steps for both NRR and HER, were calculated as displayed in Figure 2 & S11. The plots of total density of state (DOS) are shown in Figure 2a, from which the d-band centers for V-ReSe$_2$ and ReSe$_2$ are calculated to be -4.19 and -4.42 eV, respectively. It indicates the strong interaction between N$_2$/H$_2$O and V-ReSe$_2$ surface, due to more electrons distributing around Fermi level. Then, the electrons can be easily transferred to N$_2$/H$_2$O with enhanced adsorption ability of V-ReSe$_2$ toward N$_2$/H$_2$O. Additionally, the electrons of prefect surface are mainly located between Se and Re, which can be verified by the accumulated electrons (pink color area in the inset of Figure 2a) between Re and Se with the missing of one Se on V-ReSe$_2$, indicating that the electrons on prefect surface are localized and more delocalized on V-ReSe$_2$. And the delocalized electrons are readily excited to the conduction band, leading to its enhanced conductivity and the activation ability towards N$_2$ and H$_2$O molecules for accelerated NRR and HER processes. As revealed by previous reports (Figure S12),[23] three different reaction pathways are suggested for NRR catalysts, which are heavily depended on the adsorption of N$_2$. Therefore, the adsorption behavior of N$_2$ were explored, and we found that the N$_2$ was likely side-on adsorbed on ReSe$_2$ and distorted end-on adsorption on Se-vacancy sites (Figure S13 & S14). Therefore, the enzymatic mechanism of NRR processes for ReSe$_2$ and distal and alternating pathways for V-ReSe$_2$ are suggested and studied. As shown in Figure 2b, the optimized NRR processes, enzymatic pathway for ReSe$_2$ and alternating pathway V-ReSe$_2$, in the form of free energy diagrams are displayed (more details of energy data are filled in Table S3), as well as their geometric structures (more details of structures are shown in Figure S13 & S14, and coordinates of all structures are shown in the last section of the Supporting Information). Obviously, the free energy for N$_2$

adsorption on ReSe$_2$ is much higher than it on V-ReSe$_2$, suggesting that the N$_2$ would be more active on V-ReSe$_2$, which can help to accelerate the NRR processes. Specially, for V-ReSe$_2$, the free energy levels are all lower than the pathway of N$_2$ reduction on ReSe$_2$. In terms of distal pathway on V-ReSe$_2$, based on DFT calculations, the *NNH$_2$ is not the energetically preferred intermediate, for which the total energy is 0.76 eV higher than that of *HNNH. Therefore, the promising reaction mechanism for N$_2$ on V-ReSe$_2$ is the alternating pathway. These calculation results reveal the incorporated Se vacancy would activate the V-ReSe$_2$ catalyst with a highly accelerated NRR process as compared with the vacancy-free ReSe$_2$ catalyst. However, Se vacancy is also found to be effective in promoting the HER process, an intense-competing reaction towards NRR, in the V-ReSe$_2$ catalyst (Figure 2c). The free energy value is 1.45 eV for ReSe$_2$ catalyst, far away from the optimal value (ΔG_{*H} = 0 eV), and the water adsorption energy is also as high as 0.61 eV, which means that the dissociation of water is very difficult, resulting in the sluggish HER kinetics. After the incorporation of the Se vacancy, the water adsorption energy is dramatically reduced to 0.02 eV at the surface of the V-ReSe$_2$ catalyst. Meanwhile, the ΔG_{*H} value for V-ReSe$_2$ catalyst is also shifted to -0.39 eV, demonstrating it is thermodynamically favorable for *H reduction in neutral solution. As a consequence, the theoretical analysis reveals the pure vacancy engineering is not an ideal strategy for the design of NRR catalyst due to its poor selectivity between simultaneously promoted NRR and HER processes.
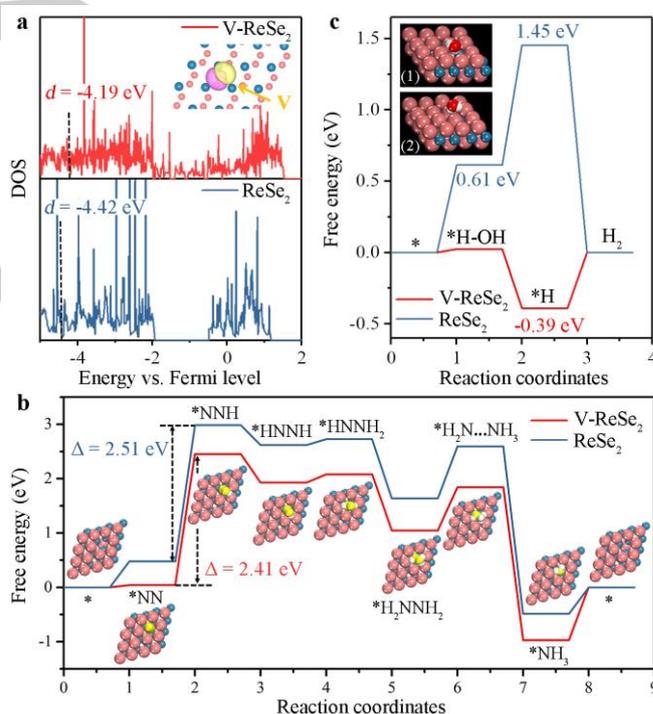

Figure 2. (a) Density of states (DOS) for V-ReSe$_2$ and ReSe$_2$ models, as well as the charge density difference of V-ReSe$_2$. Here, the pink and yellow areas present electrons accumulation and depletion, respectively. (b) Free energy diagrams for nitrogen reduction reaction on the surface of V-ReSe$_2$ and ReSe$_2$ catalysts by an associative alternating pathway. The insets show the optimized structures on V-ReSe$_2$ surface during electrocatalytic process. (c) Free energy diagrams for hydrogen evolution reaction on the surface of V-ReSe$_2$ and ReSe$_2$ catalysts. The insets show the optimized structures of water adsorption on V-ReSe$_2$ and ReSe$_2$ surfaces. Here, the adsorption site is denoted by an asterisk (*). The light-coral, blue, yellow, white, and red balls present Se, Re, N, H, and O atoms, respectively.

3

RESEARCH ARTICLE

Furthermore, the theoretical calculation results are also proved from the following experimental results, where V_r-ReSe$_2$@CBC and V_p-ReSe$_2$@CBC are used as electrocatalysts towards both NRR and HER processes. Based on three calibration curves for NH$_3$ detection by using indophenol blue, high-performance ion chromatography (HPIC), and nuclear magnetic resonance (NMR) methods (Figure S15), the ammonia contents in 0.1 M Na$_2$SO$_4$ electrolyte produced from nitrogen reduction reaction were analyzed as average values from the results of ultraviolet (UV) peaks, HPIC areas, and nuclear magnetic resonance signals. In addition, a series of blank experiments were conducted to check the purity of 0.1 M Na$_2$SO$_4$ electrolyte (Figure S16), applied N$_2$/Ar gases (Figure S17), and ^{15}N$_2$ gas (Figure S18), which all show no NH$_3$ contamination. By employing V_r-ReSe$_2$@CBC and V_p-ReSe$_2$@CBC NFs as the cathodic catalysts, the potentiostatic NRR tests were measured with continuous N$_2$ bubbling at ambient conditions. As shown in Figure 3a, the highest average NH$_3$ yields and corresponding Faradaic efficiencies (FEs) of V_r-ReSe$_2$@CBC NFs are achieved at -0.2 V versus reversible hydrogen electrode (RHE), reaching approximately 41.9 µg h^{-1} cm^{-2} and 10.2 %, respectively, which are much higher than those of V_p-ReSe$_2$@CBC NFs (7.9 µg h^{-1} cm^{-2}, FE = 6.1 %). The enhanced NRR performance of V_r-ReSe$_2$@CBC NFs is attributed to its activated electronic structure after introducing abundant Se vacancies, which displays enhanced adsorption/dissociation ability towards N-related groups (Figure 2b). As the potential gets lower than -0.2 V, the NH$_3$ yields and Faradaic efficiencies decrease significantly due to the overwhelming competition from

the HER process, while their decrease at a more positive potential of -0.1 V is originated from the limited electron to reduce N$_2$ into NH$_3$ production. In order to exclude other possibilities of NH$_3$ contaminations, such as N-contained precursor/solvent (NH$_2$OH·HCl/hydrazine hydrate) during the synthetic process, another two blank experiments were also conducted (Figure S19). In addition, the CBC nanofiber shows negative NRR performance (Figure S20), and only acts as a one-dimensional matrix to provide uniform distribution of V_r-ReSe$_2$ nanosheets for enhanced charge transfer ability, leading to higher NH$_3$ production as compared with the corresponding bulk (Figure S21). The outstanding performance of as-obtained V_r-ReSe$_2$@CBC NFs is comparable with the NH$_3$ yields and Faradaic efficiencies of previous electrocatalysts (Table S4). Meanwhile, no hydrazine is detected in the electrolyte (Figure S22), proving the high selectivity of V_r-ReSe$_2$@CBC NFs. As displayed in Figure S23, both the average NH$_3$ yields and Faradaic efficiencies maintain at a stable level without obvious fluctuation, which demonstrates good potential for industrial applications of the catalysts. However, the V_r-ReSe$_2$@CBC NFs also show an enhanced electrocatalytic performance towards hydrogen evolution reactions (Figure S24), which matches well with the DFT calculation results (Figure 2c). In detail, the V_r-ReSe$_2$@CBC NFs show lower onset overpotential (η = 178 mV) and Tafel slope (75 mV dec^{-1}) than those for V_p-ReSe$_2$@CBC NFs (η = 245 mV; Tafel slope: 85 mV dec^{-1}), demonstrating the positive role of selenium vacancy towards hydrogen evolution reactions.
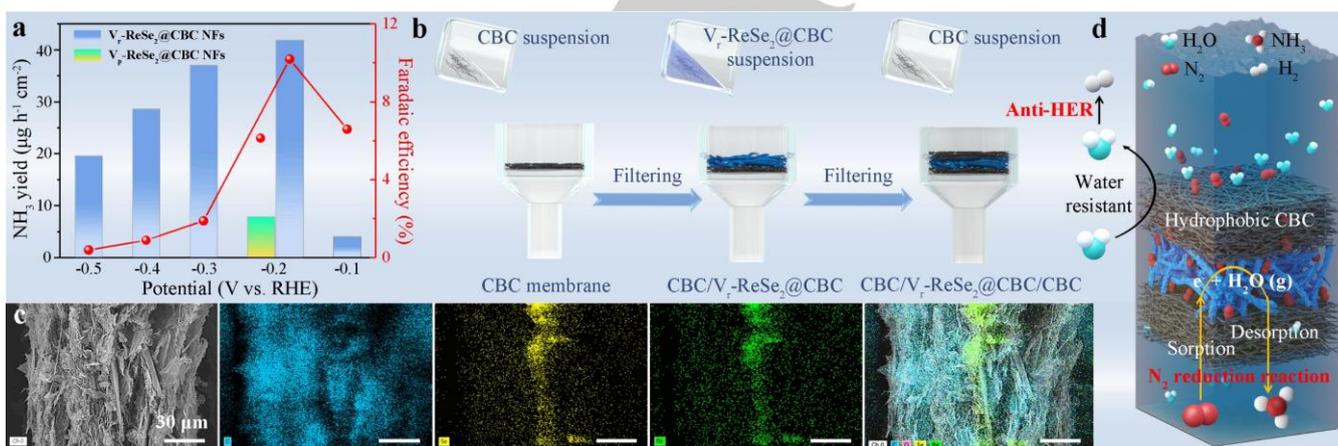

Figure 3. (a) Electrocatalytic NRR performance with NH$_3$ yield (bar graph) and Faradaic efficiency (red point) for V_r-ReSe$_2$@CBC and V_p-ReSe$_2$@CBC NFs in 0.1 M Na$_2$SO$_4$ electrolyte under ambient conditions. (b) Schematic illustration for the preparation of "sandwich"-structured CBC/V_r-ReSe$_2$@CBC/CBC membrane. (c) EDX elemental mapping images of CBC/V_r-ReSe$_2$@CBC/CBC membrane with C, Se, Re, and mixed elements. The scale bar: 30 µm. (d) Proposed overall mechanism for the selective and enhanced electrochemical NRR process by encapsulating V_r-ReSe$_2$@CBC NFs within hydrophobic CBC layers.

Therefore, vacancy engineering is revealed as an underutilized strategy with poor NRR selectivity, which would boost not only NRR but also HER processes from both theoretical and experimental results. In order to suppress competing HER and increase the Faradaic efficiency for NRR, a "sandwich"-structured CBC/V_r-ReSe$_2$@CBC/CBC membrane was constructed by encapsulating V_r-ReSe$_2$@CBC NFs between two hydrophobic CBC layers (Figure 3b) after filtering CBC, V_r-ReSe$_2$@CBC, and CBC suspensions *via* a layer by layer process (mass ratio for the three components is 1:1:1). The prepared CBC/Vr-ReSe$_2$@CBC/CBC membrane is displayed in Figure S25, which

possesses extraordinary flexibility as an electrode for nitrogen reduction reactions. As the EDX elemental mapping images of its cross-section shown in Figure 3c, the V_r-ReSe$_2$@CBC NFs are uniformly buried under the coverage of two-side hydrophobic CBC layers. The CBC layers make it possible to achieve a hydrophobic interior of V_r-ReSe$_2$@CBC with trace vaporized water, thus impeding HER process with reduced Faradaic efficiency. Consequently, abundant humid N$_2$ gas would infuse into the V_r-ReSe$_2$@CBC NFs and concentrate near its surface driven by the thermodynamically favorable sorption,[40] leading to the enhanced NRR process with possibly high Faradaic efficiency.

RESEARCH ARTICLE

As displayed in Figure 4a, the highest average NH_3 yield and corresponding Faradaic efficiency for CBC/V_r-ReSe$_2$@CBC/CBC membrane are achieved to be 28.3 µg h^{-1} cm^{-2} and 42.5 %, respectively, when the negative potential reaches to -0.25 V. The four-fold increase in Faradaic efficiency for NRR can originate from the anti-hydrogen evolution reaction with the existence of two-side hydrophobic CBC layers (Figure 3d), making more supplied electrons to reduce nitrogen molecules. Additionally, the impeded HER process in CBC/V_r-ReSe$_2$@CBC/CBC membrane can also be proved from its significantly reduced current density, negatively shifted onset overpotential, and higher Tafel slope as compared with those for V_r-ReSe$_2$@CBC NFs (Figure S26). As the potential is more negative than -0.25 V, both the NH_3 yield and Faradaic efficiency decrease continuously, as the hydrophobicity of CBC/V_r-ReSe$_2$@CBC/CBC membrane is changed into a hydrophilic character under high negative voltage according to previous reports,[41] thus leading to the revitalization of hydrogen evolution reaction as an overwhelming competition. Although the NH_3 yield at -0.15 V decreases to 3.2 µg h^{-1} cm^{-2} sharply (due to the limited electron to reduce N_2 into NH_3), the Faradaic efficiency still maintains at a high level of 35.3% attributing to the excellent hydrophobicity of CBC layer at this potential. In spite of ruling out the possible NH_3 contaminations from the electrocatalyst itself (Figure S19), a ^{15}N isotopic labeling experiment (Figure 4b) was further used to confirm the ammonia production. The ^1H NMR spectra of commercial ($^{14}NH_4$)$_2SO_4$ and ($^{15}NH_4$)$_2SO_4$ samples were collected as standard spectra. In particular, the ^1H NMR spectra for the electrolytes after the electrocatalytic process at -0.25 V show a ^{14}N triplet (I = 1) and a ^{15}N doublet (I = ½) in the range of 6.85–7.15 ppm, respectively. The peak positions for both triplet and doublet closely match the reference substance of ($^{14}NH_4$)$_2SO_4$ and ($^{15}NH_4$)$_2SO_4$, thus demonstrating the successful production of ammonia during the NRR process. Additionally, when $^{15}N_2$ gas was used as a feedstock, the corresponding ^1H NMR spectrum reveals distinguishable chemical shifts as standard ($^{15}NH_4$)$_2SO_4$ without obvious peaks for the ^{14}N triplet, demonstrating that the detected ammonia completely derived from the supplied $^{15}N_2$.

To further evaluate the reaction kinetics of the CBC/V_r-ReSe$_2$@CBC/CBC membrane as a NRR electrocatalyst, a series of electrocatalytic tests were conducted under different nitrogen flow rates and reaction temperatures. As shown in Figure 4c, both the NH_3 yield and Faradaic efficiency were maintained at almost unchanged values regardless of various nitrogen flow rates, indicating the N_2 diffusion process becomes a non-rate-determining step due to the existence of porous and hydrophobic CBC layers. Moreover, the NH_3 yield increases by 2.57 times when the NRR temperature increased from 0 °C to 60 °C (Figure 4d), which demonstrates that the mass transfer is a critical factor for accelerated NH_3 production rate by using CBC/V_r-ReSe$_2$@CBC/CBC membrane as the electrocatalyst. In accordance with the Arrhenius equation and Arrhenius plot (Figure S27), the apparent activation energy of CBC/V_r-ReSe$_2$@CBC/CBC membrane for NRR process is calculated as 12.1 kJ mol^{-1}, demonstrating its low energy cost as compared with the energy-intensive Haber-Bosch process.

To reveal the structural advantages of two-side hydrophobic layers for nitrogen bubble absorption, nitrogen bubble adhesive force measurements for both V_r-ReSe$_2$@CBC and CBC/V_r-ReSe$_2$@CBC/CBC membranes were investigated by using one nitrogen bubble (in 0.1 M Na_2SO_4 electrolyte) to touch their under-electrolyte surfaces,[42] respectively. As a result, there is only a weak adhesive force between the nitrogen bubble and the measured surface of V_r-ReSe$_2$@CBC membrane (Figure 5a) while a strong bubble adhesive force is measured on the surface of CBC/V_r-ReSe$_2$@CBC/CBC membrane (Figure 5b), which is further demonstrated through the appreciable deformation of the nitrogen bubble during the corresponding measurement process (insets 1-3 of Figure 5). The bubble contact angles reach 140.9° ± 2.1° and 137.7° ± 2.3° on the surfaces of V_r-ReSe$_2$@CBC and CBC/V_r-ReSe$_2$@CBC/CBC membranes under electrolyte (insets 4), respectively. Additionally, surface superhydrophilicity of the V_r-ReSe$_2$@CBC membrane is shown in inset 5 of Figure 5a, when the infiltrated electrolyte droplet was immediately put into the membrane. Attributable to the protection from the CBC layers, the CBC/V_r-ReSe$_2$@CBC/CBC membrane processes a dramatically enhanced hydrophobicity (inset 5 of Figure 5b), which is beneficial to suppressing the hydrogen evolution reaction by restricting the contact between electrocatalytic V_r-ReSe$_2$@CBC interior and aqueous electrolyte. The abrupt three-phase interface provides a discontinuous state with abundant free electroactive sites for enhanced NRR process.
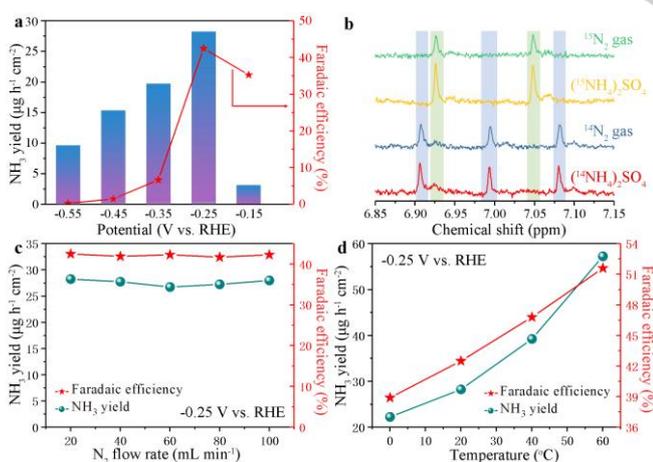

Figure 4. (a) Electrocatalytic NRR performance with NH_3 yield (bar graph) and Faradaic efficiency (red star) for CBC/V_r-ReSe$_2$@CBC/CBC membrane under ambient condition. (b) ^1H NMR analysis of the membrane fed by $^{14}N_2$ and $^{15}N_2$ gases after electrochemical NRR process. NH_3 yield and Faradaic efficiency under (c) different N_2 flow rates and (d) temperatures at -0.25 V *vs*. RHE.
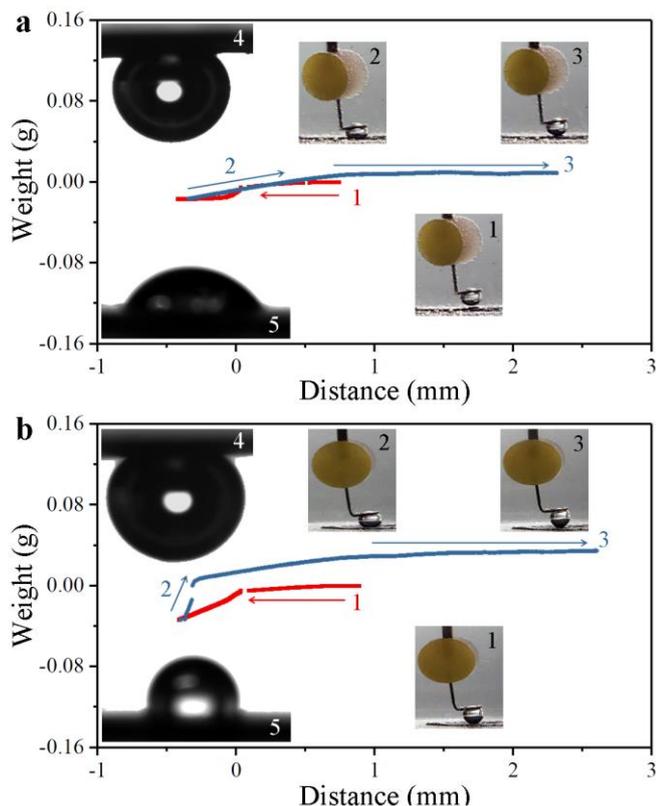
5

RESEARCH ARTICLE

Figure 5. Under-electrolyte (0.1 M Na_2SO_4) nitrogen bubble adhesive force and superhydrophilic measurements. (a–b) Nitrogen bubble adhesive force measurements of V_r-$ReSe_2$@CBC and CBC/V_r-$ReSe_2$@CBC/CBC membranes. The V_r-$ReSe_2$@CBC membrane obviously shows weak bubble adhesive force (~32 mg) while the strong bubble adhesive force is measured on CBC/V_r-$ReSe_2$@CBC/CBC membrane (~88 mg). The insets 1-3 show different bubble states during the corresponding measurement process for adhesive force, where process 1 displays the nitrogen bubble gets close to the electrode surface, process 2 illustrates the nitrogen bubble touches with electrode surface, and process 3 demonstrates the nitrogen bubble separates from the electrode surface, respectively. The nitrogen bubble contact angles under electrolyte were measured as 140.9° ± 2.1° and 137.7° ± 2.3° for V_r-$ReSe_2$@CBC and CBC/V_r-$ReSe_2$@CBC/CBC membranes (insets 4), respectively. For inset 5, the wetting ability of the membranes in Na_2SO_4 solution droplets demonstrates the surface hydrophobicity of CBC/V_r-$ReSe_2$@CBC/CBC membrane.

Furthermore, COMSOL Multiphysics simulations were performed to reveal the advantages of covered hydrophobic CBC layer by constructing a three-dimensional model in Figure S28a, where the V_r-$ReSe_2$@CBC was adhered on the one-side of hydrophobic and porous CBC layer with a cuboid shape (0.25 × 0.04 × 0.07 m). As shown in Figure S28b, the voltage and the H^+ concentration in the right boundary of the model are fixed as 5.5 V and 0.1 mmol m^{-3}, with continuous diffusion of H^+ ions from right to left boundaries for nitrogen reduction reactions. In detail, the COMSOL Multiphysics simulations were conducted by using secondary current distribution and transport of diluted species modules with more details in the Supporting Information. As plotted in Figure 6a, the voltage at the most left-band side boundary of the V_r-$ReSe_2$@CBC interface maintains at a higher but stable value of ~5.6 V, when the internal diffusion reaches to an equilibrium within 5.5 s of the reaction time. Meanwhile, the concentration of H^+ ions at the most left side boundary of the V_r-$ReSe_2$@CBC interface is close to zero with the increase of reaction time (Figure 6b), indicating the fast hydrogen coupling

process with nitrogen molecules to realize rapid ammonia production. The rapid equilibriums within 5.5 s for both the voltage and concentration of H^+ ions at the left-band side boundary of electrocatalytic V_r-$ReSe_2$@CBC demonstrate the hydrophobic and porous CBC layer would not significantly affect the NRR process with plenty of N_2 source. Then, the distribution of various parameters in the electrode, including voltage, current density and concentration of H^+ ions, are shown in Figure 6c-6e when the reaction time is 5.5 s. The voltages in the boundary of the hydrophobic and porous CBC layer (right side of the model) and the left boundary of V_r-$ReSe_2$@CBC interface are calculated to be 5.99 and 5.58 V [based on Equation (4) in the Supporting Information], respectively, with a slight difference of 0.41 V (Figure 6c). This slight voltage reduction is attributed to the high conductivity of the well-connected CBC nanofibers, which ensures enough supplied electrons to reduce nitrogen on the electrocatalytic V_r-$ReSe_2$@CBC interface with low energy dissipation from internal resistance. Meanwhile, the current density near the electrocatalytic V_r-$ReSe_2$@CBC interface is slightly higher than those in the right region of CBC layer (Figure 6d), where the arrow lines imply the direction of current density change. The narrow change of the current density is also attributed to the high conductivity of CBC nanofibers with enhanced NRR process near the V_r-$ReSe_2$@CBC interface. The H^+ concentration near the interface of V_r-$ReSe_2$@CBC decreases dramatically (Figure 6e), which indicates the possible resistance towards water molecules as the hydrophobic and porous properties for as-covered CBC layer on the top of V_r-$ReSe_2$@CBC. As a result, only limited electrolyte could be in contact with the interface of electrocatalytically active V_r-$ReSe_2$@CBC, resulting in suppressed HER process with more unused active sites for NRR in the CBC/V_r-$ReSe_2$@CBC/CBC membrane.
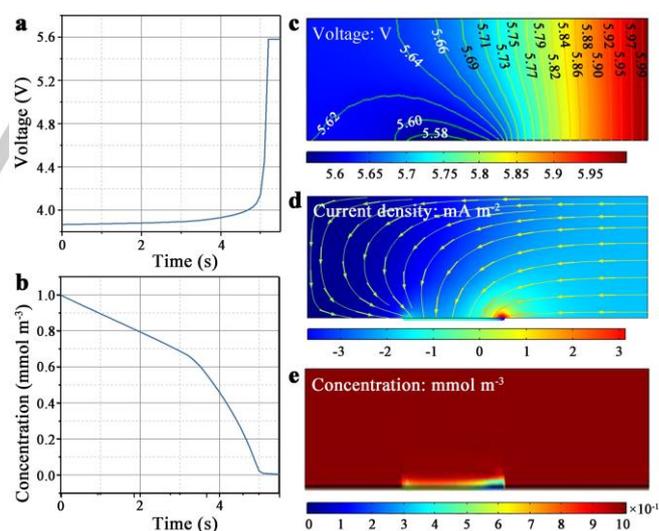

Figure 6. The changes of (a) voltage and (b) concentration (H^+ ions) in the simulated electrodes with a hydrophobic and porous surface within 5.5 s in the most left boundary of the V_r-$ReSe_2$@CBC. The distributions of (c) voltage, (d) current density, and (e) concentration of H^+ ions in the electrode when the reaction time is 5.5 s.

Conclusion

RESEARCH ARTICLE

In summary, we have prepared a "sandwich"-structured CBC/V$_r$-ReSe$_2$@CBC/CBC membrane with hydrophobic surface and high electroactivity. As predicted by the DFT calculation results, the introduced selenium vacancy could modulate the electronic structures of ReSe$_2$ nanosheet by positively shifting its d-band position, which shows poor electrocatalytic selectivity with simultaneously enhanced NRR and HER processes. As revealed by the under-electrolyte nitrogen bubble adhesive force and superhydrophilic measurements, the covered hydrophobic CBC layer is beneficial to resisting the intimate contact between water molecules and V$_r$-ReSe$_2$@CBC nanofibers, and slightly increases the adhesive force towards nitrogen bubbles. As a result, the CBC/V$_r$-ReSe$_2$@CBC/CBC membrane displayed a boosted Faradaic efficiency by ~32% at room temperature. As revealed by COMSOL Multiphysics stimulations, the porous and hydrophobic CBC layers could provide special channels for sluggish internal diffusion of H$^+$ ions, leaving limited water molecules to contact the electro-active V$_r$-ReSe$_2$@CBC nanofibers and more unoccupied active site for nitrogen adsorption and NRR processes. This work provides a possible strategy to ameliorate potentially active NRR catalysts by constructing a three-phase boundary at an abrupt interface.
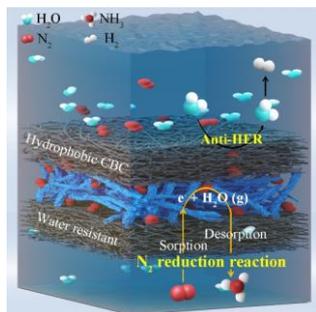
Acknowledgements

[1] J. W. Erisman, M. A. Sutton, J. Galloway, Z. Klimont, W. Winiwarter, *Nat. Geosci.* **2008**, *1*, 636-639.

[2] B. M. Hoffman, D. Lukoyanov, Z. Y. Yang, D. R. Dean, L. C. Seefeldt, *Chem. Rev.* **2014**, *114*, 4041-4062.

[3] M. A. Lgar, G. Blanger-Chabot, R. D. Dewhurst, E. Welz, I. Krummenacher, B. Engels, H. Braunschweig, *Science* **2018**, *359*, 896-900.

[4] A. Klerke, C. H. Christensen, J. K. Nørskov, T. Vegge, *J. Mater. Chem.* **2008**, *18*, 2304-2310.

[5] A. E. Shilov, *Russ. Chem. Bull.* **2003**, *52*, 2555-2562.

[6] C. D. Lv, C. S. Yan, G. Chen, Y. Ding, J. X. Sun, Y. S. Zhou, G. H. Yu, *Angew. Chem. Int. Ed.* **2018**, *57*, 6073-6076; *Angew. Chem.* **2018**, *130*, 6181-6184.

[7] J. N. Renner; L. F. Greenlee, A. M. Herring, K. E. Ayers, *Electrochem. Soc.* **2015**, *24*, 51-57.

[8] C. J. M. Vander Ham, M. T. M. Koper, D. G. H. Hetterscheid, *Chem. Soc. Rev.* **2014**, *43*, 5183-5191.

[9] X. Chen, N. Li, Z. Kong, W. J. Ong, X. Zhao, *Mater. Horiz.* **2018**, *5*, 9-27.

[10] K. C. Macleod, P. L. Holland, *Nat. Chem.* **2013**, *5*, 559-565.

[11] C. Guo, J. Ran, A. Vasileff, S. Z. Qiao, *Energy Environ. Sci.* **2018**, *11*, 45-56.

[12] Z. W. Seh, J. Kibsgaard, C. F. Dickens, I. Chorkendorff, J. K. Nrskov, T. F. Jaramillo, *Science* **2017**, *355*, eaad4998.

[13] M. A. Shipman, M. D. Symes, *Catal. Today* **2017**, *286*, 57-68.

[14] K. H. Liu, H. X. Zhong, S. L. Li, Y. X. Duan, M. M. Shi, X. B. Zhang, J. M. Yan, Q. Jiang, *Prog. Mater. Sci.* **2018**, *92*, 64-111.

[15] S. Licht, B. Cui, B. Wang, F.-F. Li, J. Lau, S. Liu, *Science* **2014**, *345*, 637-640.

[16] G.-F. Chen, X. Cao, S. Wu, X. Zeng, L.-X. Ding, M. Zhu, H. Wang, *J. Am. Chem. Soc.* **2017**, *139*, 9771-9774.

[17] H. P. Jia, E. A. Quadrelli, *Chem. Soc. Rev.* **2014**, *43*, 547-564.

[18] S. Chen, S. Perathoner, C. Ampelli, C. Mebrahtu, D. Su, G. Centi, *Angew. Chem. Int. Ed.* **2017**, *56*, 2699-2703; *Angew. Chem.* **2017**, *129*, 2743-2747.

[19] L. M. Azofra, N. Morlanés, A. Poater, M. K. Samantaray, B. Vidjayacoumar, K. Albahily, L. Cavallo, J.-M. Basset, *Angew. Chem. Int. Ed.* **2018**, *57*, 15812-15816; *Angew. Chem.* **2018**, *130*, 16038-16042.

[20] Y. Yao, S. Zhu, H. Wang, H. Li, M. Shao, *J. Am. Chem. Soc.* **2018**, *140*, 1496-1501.

[21] F. L. Lai, N. Chen, X. B. Ye, G. J. He, W. Zong, K. B. Holt, B. C. Pan, I. P. Parkin, T. X. Liu, R. J. Chen, *Adv. Funct. Mater.* **2020**, *30*, 1907376.

[22] H. Cheng, L.-X. Ding, G.-F. Chen, L. L. Zhang, J. Xue, H. H. Wang, *Adv. Mater.* **2018**, *30*, 1803694.

[23] X. H. Li, T. S. Li, Y. J. Ma, Q. Wei, W. B. Qiu, H. R. Guo, X. F. Shi, P. Zhang, A. M. Asiri, L. Chen, B. Tang, X. P. Sun, *Adv. Energy Mater.* **2018**, *8*, 1801357.

[24] E. Skúlason, T. Bligaard, S. Gudmundsdóttir, F. Studt, J. Rossmeisl, F. Abild-Pedersen, T. Vegge, H. Jónssonac, J. K. Nørskov, *Phys. Chem. Chem. Phys.* **2012**, *14*, 1235-1245.

[25] H. K. Lee, C. S. L. Koh, Y. H. Lee, C. Liu, I. Y. Phang, X. M. Han, C.-K. Tsung, X. Y. Ling, *Sci. Adv.* **2018**, *4*, eaar3208.

[26] J. F. Xie, H. Zhang, S. Li, R. X. Wang, X. Sun, M. Zhou, J. F. Zhou, X. W. Lou, Y. Xie, *Adv. Mater.* **2013**, *25*, 5807-5813.

[27] J. F. Xie, J. J. Zhang, S. Li, F. Grote, X. D. Zhang, H. Zhang, R. X. Wang, Y. Lei, B. C. Pan, Y. Xie, *J. Am. Chem. Soc.* **2013**, *135*, 17881-17888.

[28] Q. Zhang, W. J. Wang, X. Kong, R. G. Mendes, L. W. Fang, Y. H. Xue, Y. Xiao, M. H. Rümmeli, S. L. Chen, L. Fu, *J. Am. Chem. Soc.* **2016**, *138*, 11101−11104.

[29] V. Babentsov, R. B. James, *J. Cryst. Growth* **2013**, *379*, 21-27.

[30] D. J. Keeble, E. A. Thomsen, A. Stavrinadis, I. D. W. Samuel, J. M. Smith, A. A. R. Watt, *J. Phys. Chem. C* **2009**, *113*, 17306-17312.

[31] Y. Sun, J. Meng, H. X. Ju, J. F. Zhu, Q. X. Li, Q. Yang, *J. Mater. Chem. A* **2018**, *6*, 22526-22533.

[32] A. J. Almeida, A. Sahu, A. Riedinger, D. J. Norris, M. S. Brandt, M. Stutzmann, R. N. Pereira, *J. Phys. Chem. C* **2016**, *120*, 13763–13770.

[33] Z. Y. Wu, D. C. Xian, T. D. Hu, Y. N. Xie, Y. Tao, C. R. Natoli, E. Paris, A. Marcelli, *Phys. Rev. B* **2004**, *70*, 033104.

[34] F. Hilbrig, C. Michel, G. L. Haller, *J. Phys. Chem.* **1992**, *96*, 9893.

[35] M. Fröba, K. Lochte, W. Metz, *J. Phys. Chem. Solids* **1996**, *57*, 635.

[36] D. E. Sayers, E. A. Stern, F. W. Lytle, *Phys. Rev. Lett.* **1971**, *27*, 1204.

[37] Z. Sun, Q. Liu, T. Yao, W. Yan, S. Q. Wei, *Sci. China Mater.* **2015**, *58*, 313-341.

[38] C. L. Tan, Z. M. Luo, A. Chaturvedi, Y. Q. Cai, Y. H. Du, Y. Gong, Y. Huang, Z. C. Lai, X. Zhang, L. R. Zheng, X. Y. Qi, M. H. Goh, J. Wang, S. K. Han, X.-J. Wu, L. Gu, C. Kloc, H. Zhang, *Adv. Mater.* **2018**, *30*, 1705509.

[39] H. Funke, A. Scheinost, M. Chukalina, *Phys. Rev. B* **2005**, *71*, 094110.

[40] H. K. Lee, Y. H. Lee, J. V. Morabito, Y. Liu, C. S. L. Koh, I. Y. Phang, S. Pedireddy, X. Han, L.-Y. Chou, C.-K. Tsung, X. Y. Ling, *J. Am. Chem. Soc.* **2017**, *139*, 11513–11518.

[41] A. Quinn, R. Sedev, J. Ralston, *J. Phys. Chem. B* **2003**, *107*, 1163-1169.

[42] Y. Huang, M. J. Liu, J. X. Wang, J. M. Zhou, L. B. Wang, Y. L. Song, L. Jiang, *Adv. Funct. Mater.* **2011**, *21*, 4436-4441.

RESEARCH ARTICLE

Entry for the Table of Contents

Insert graphic for Table of Contents here.

N_2 Electroreduction to NH_3 via Selenium Vacancy-Rich $ReSe_2$ Catalysis at an Abrupt Interface.